Ocean Sci. Discuss., 10, 1807–1831, 2013
www.ocean-sci-discuss.net/10/1807/2013/
doi:10.5194/osd-10-1807-2013

Ocean Science
Discussions
Open Access

Eddy length scales and the Rossby radius in the Arctic Ocean

A. J. G. Nurser and S. Bacon

National Oceanography Centre, Southampton, UK

Received: 25 September 2013 – Accepted: 3 October 2013 – Published: 22 October 2013

Correspondence to: S. Bacon (s.bacon@noc.ac.uk)

Published by Copernicus Publications on behalf of the European Geosciences Union.

Abstract

The first (and second) baroclinic deformation (or Rossby) radii are presented and discussed north of ∼60° N, focusing on deep basins and shelf seas in the high Arctic Ocean, the Nordic Seas, Baffin Bay, Hudson Bay and the Canadian Arctic Archipelago, derived from high-resolution ice-ocean general circulation model output. Comparison of the model output with measured results shows that low values of the Rossby radius (in shallow water) and high values (in the Canada Basin) are accurately reproduced, while intermediate values (in the region of the Makarov and Amundsen Basins) are overestimated. In the high Arctic Ocean, the first Rossby radius increases from ∼5 km in the Nansen Basin to ∼15 km in the central Canadian Basin. In the shelf seas and elsewhere, values are low (1–7 km), reflecting weak density stratification, shallow water, or both. Seasonality only strongly impacts the Rossby radii in shallow seas where winter homogenisation of the water column can reduce it to the order of 100 m. We also offer an interpretation and explanation of the observed scales of Arctic Ocean eddies.

1 Introduction

The first baroclinic Rossby radius of deformation is of fundamental importance in atmosphere-ocean dynamics. It is the horizontal scale at which rotation effects become as important as buoyancy effects, and is the "natural" scale of boundary currents, eddies and fronts (Gill, 1982; Chelton et al., 1998; Saenko, 2006). In the context of ocean models, it is important to know the field of the Rossby radius so that we know where models will describe boundary currents and the eddy field adequately and where they will not. For example, two gridpoints per eddy radius are necessary to adequately resolve the eddies, and one gridpoint per radius to "permit" them, while the typical best resolution in oceanic general circulation models (OGCMs) is currently ∼0.1° (ca. 10 km). In the deeper waters of the Arctic Ocean and over much of the Nordic Seas, stratification is generally weak, so the Rossby radius is typically 5–15 km instead of the

OSD
10, 1807–1831, 2013

30–50 km characteristic of the mid-latitude oceans, so OGCMs are (typically) eddy-permitting at best. Over the broad Arctic Ocean shelf seas, the Rossby radius is even smaller, and here OGCMs are not even eddy-permitting. Chelton et al. (1998) describe the quasi-global geographical variability of the first baroclinic Rossby radius, but their analysis does not extend north of ~60° N. This motivates the present study.

2 Methods and data

The standard method of finding the internal deformation (Rossby) radii involves solving the linearized quasi-geostrophic potential vorticity equation, and is described by Chelton et al. (1998). Briefly, solutions for the velocity are separated into horizontal and vertical components, where the structure of the vertical velocity $\phi(z)$ must satisfy

$$N^{-2}(z)\frac{\mathrm{d}^2\phi}{\mathrm{d}z^2} = c^{-2}\phi \tag{1}$$

with N the buoyancy frequency where

$$N^{-2} = -\frac{g}{\rho_{\mathrm{ref}}}\frac{\partial\rho}{\partial z} = g\left(\alpha\frac{\partial\theta}{\partial z} - \beta\frac{\partial S}{\partial z}\right) \tag{2}$$

Here $\rho = \rho(z)$ is the potential density profile, ρ_{ref} is a reference density, and α and β are the thermal expansion and haline contraction coefficients (Gill, 1982). The boundary conditions to be satisfied are zero vertical velocity at the surface and ocean floor:

$$\phi = 0 \text{ at } z = -H, z = 0 \tag{3}$$

where H is ocean depth. Solutions are only possible for certain values of c^{-2} (the eigenvalues). The corresponding c_i (decreasing with increasing i) are then the phase speeds of the internal gravity waves, for internal modes $i = 1, 2, \ldots$, while the Rossby radii R_i are

$$R_i = c_i/|f| \tag{4}$$

OSD
10, 1807–1831, 2013

where $f = 2\Omega \sin\theta$ is the Coriolis parameter for Earth rotation rate Ω and latitude θ. The c_i may be found exactly by numerically integrating Eq. (1) to find values of c that satisfy the conditions of Eq. (3). Variations in f have little influence on R_i within the Arctic Ocean and Nordic Seas: sin (90°, 80°, 70°, 60°) = (1, 0.985, 0.940, 0.866); but are, of course, important in reducing the deformation radius from low to high latitudes.

Note that in the presence of sloping topography, the vertical velocity need not be zero on the ocean floor, so the conditions of Eq. (3) no longer hold, and the vertical and horizontal structures become coupled; cf. Killworth and Blundell (1999). However, the resulting equations become very complex, and the link between the fastest internal gravity wave speed c_1 and the scale of maximum eddy growth becomes less clear, so here we present the simple flat-bottomed solutions.

We calculate the fields of the internal Rossby radius from the temperature and salinity fields produced by the OCCAM global 1/12° model (Marsh et al., 2009). The model has 66 levels in the vertical and includes 27 levels in the upper 400 m with thickness ranging from 5.4 m in the uppermost layer to 48 m at 400 m and to 103 m at 1000 m. In the Arctic, this model was initialized with a dataset merged from the World Ocean Atlas and the Arctic Ocean Atlas (Steele et al., 2001). It was then run from 1985–2004 (Marsh et al., 2009) using surface fluxes generated from bulk formulae using model sea surface temperature and atmospheric output from the US National Centers for Climate Research, together with satellite solar forcing and precipitation. The OCCAM model bathymetry (Fig. 1) is derived from the bathymetry of Smith and Sandwell (1997), patched north of 72.0° N with the International Bathymetric Chart of the Arctic Ocean (IBCAO) dataset (Jakobsson et al., 2000); see Aksenov et al. (2010a) for further details.

The usefulness of OCCAM in the Arctic has been demonstrated in a series of recent papers: Aksenov et al. (2010a, 2010b, 2011) describe the Atlantic water inflows, the polar water outflows, and the representation of the Arctic Circumpolar Boundary Current in the model. We use OCCAM output for a number of reasons. The model has high horizontal and vertical resolution, and realistic coastlines, so it interpolates and (to some extent) extrapolates the climatological initialisation, e.g. in providing winter data.

OSD
10, 1807–1831, 2013

The model imposes dynamical consistency throughout the domain, and by choosing output a few years from the start of the run (here we diagnose 1992), any inconsistencies associated with spin-up are avoided. Furthermore, Aksenov et al. (2010a, Fig. 1) show that global mean kinetic energy stabilises after a few years, so that the model's dynamical state is close to equilibrium, while the thermodynamic state has drifted little from the initial conditions.

To assess the validity of the model results, we compare with the Rossby radius calculated from geographically-representative ocean data. In particular, we use (i) the Oden 1991 expedition (Anderson et al., 1994), and (ii) the Arctic Ocean Section 1994 expedition (Carmack et al., 1997). These two expeditions combine to provide a trans-basin, Alaska–Svalbard, section, but they skirt the western edge of the Canada Basin, so for completeness, we also include (iii) the Beaufort Gyre Exploration Project 2003 expedition (Proshutinsky et al., 2009). The three data sets provide surface-to-bottom profiles of temperature and salinity from the Nansen, Amundsen, Makarov and Canada Basins. Station locations are shown in Fig. 2. Data were obtained (i, ii) from the World Ocean Database, hosted by the US National Oceanographic Data Center, http://www.nodc.noaa.gov/, and (iii) from the BGEP website, http://www.whoi.edu/beaufortgyre/.

3 Results

3.1 Comparison of model and data results

For the three selected expeditions, AOS'94, Oden'91 and BG2003, exact calculations of co-located model and data mode 1 Rossby radius are shown in Fig. 3. Allowing for some scatter, is it first noted that the smallest values (in the shallow waters, offshore Alaska and Svalbard) and the largest values (in the Beaufort Gyre) are accurately reproduced by the model. Starting from the Chukchi Sea, the model results begin to diverge from the data in the region west of the Chukchi Cap; in the Makarov Basin (in

OSD
10, 1807–1831, 2013

the vicinity of AOS'94 stations 20–35), the model typically overestimates by ∼4 km. On the Eurasian side of the North Pole, the difference reduces, becoming ∼2 km in the Amundsen Basin (in the vicinity of Oden'91 stations 10–40), before returning to close agreement as the section approaches Svalbard (Oden'91, after station 40).

Inspection of representative model and data temperature and salinity profiles (Fig. 4) shows the cause of this divergence. The model reproduces the observed temperature profiles quite well: vertical gradients are smoother than observed, and the Atlantic Water temperature maximum is a little deeper than observed, but inaccuracies of order 0.1 °C would make little difference to the vertical density gradients. The cause of the model over-estimation of central Arctic Ocean Rossby radii is found in the upper-ocean salinity distribution. While the model vertical salinity gradients are realistic, the modeled surface layer is approximately 100 m too deep, leading to salinities being too fresh by ∼1 in the upper 200–300 m, which in turn increases the vertical density stratification, hence also the buoyancy frequency, and therefore the Rossby radius.

The model generates over-estimates of intermediate values of the Rossby radius in the central Arctic Ocean, of ∼30 % in the Makarov Basin and 10–20 % in the Amundsen Basin. However, previous publications (cited in Sect. 2) have shown the model circulation to be realistic, so the model patterns of the Rossby radius are realistic, and the magnitudes are realistic at high and low ends, so we proceed to examine the model results from that perspective.

3.2 Model fields (exact and approximate solutions)

The first mode wave speed (c_1) and Rossby radius (R_1) for winter and summer (March and August) are shown in Figs. 5 and 6. They vary substantially over the Arctic geographically. In the deep basins of the Arctic Ocean, they increase quasi-monotonically, with typical values of R_1 ranging from ∼6 km in the Nansen Basin, through 9–10 km in the Amundsen Basin, 11 km in the Makarov Basin, to the largest values of ∼15 km, found towards the centre of the Canadian Basin. The deep Nordic Seas are divided by the mid-basin ridge system. The Norwegian Sea (to the east) contains the Atlantic-

OSD
10, 1807–1831, 2013

dominated inflows, where $R_1 \sim 7$ km. The Iceland and Greenland Seas (to the west) contain the polar-dominated outflows, where $R_1 \sim 3$ km. All the shallow shelf seas show very small values of R_1 – generally less than 2 km, and in places, significantly less than 1 km. The seasonal variation is less pronounced; the main differences are seen over the Eurasian shelf seas, where R_1 is generally lower in winter than in summer.

The model also resolves the second mode Rossby radius (R_2), and we plot it and its wave speed (c_2) for March 1992 (Fig. 7). We do not show August results because the mode 2 seasonal differences are similar to those for mode 1. As would be predicted (cf. Sect. 4), the mode 2 amplitudes are roughly half of those of mode 1, and the contrast between shallow shelf seas and deep ocean is similar. However, the mode 2 structure is subtly different that of mode 1, in that the trans-polar increasing tendency is largely absent from c_2 and R_2. We provide a summary of our results in Table 1 by calculating summer and winter averages of R_1 and R_2 for the areas shown in Fig. 8.

We also calculated the Rossby radius using the (approximate) WKBJ/LG method (eg. Chelton et al., 1998). Where ϕ varies in the vertical more rapidly than N, the c_i can be well approximated by

$$c_i = (\pi i)^{-1} \int_{-H}^{0} N \mathrm{d}z \tag{5}$$

where H is the water depth. Although over much of the ocean N varies too rapidly for this method to be formally valid, Chelton et al. (1998) found that this WKBJ/LG approximation worked surprisingly well in generating a global climatology of the first internal mode Rossby radius, R_1. We plot the exact field minus the approximate field for the wave speed and Rossby radius of modes 1 and 2 for March and August 1992 in Fig. 9. In the deep basins, the WKBJ/LG method is in error typically by ±1–2 km, or ∼20 %. Over the shelf seas, the accuracy of the approximation is much reduced, generally substantially under-estimating the Rossby radius.

OSD
10, 1807–1831, 2013

3.3 Rossby radius and stratification

The wide range of values of Rossby radii throughout the Arctic Ocean are a result of the interplay between density stratification and water depth, with the former largely (but not exclusively) controlled by upper-ocean salinity variability. We illustrate this as follows. Equation (5) can be further approximated assuming constant N (Gill, 1982):

$$c_i = \frac{NH}{i\pi} \tag{6}$$

Carmack (2000) illustrates the evolution of mean profiles of potential temperature and salinity by basin within the deep Arctic Ocean. In progressing across the Arctic from the Nansen to the Canadian Basin, the upper-ocean salinity steadily decreases. Since salinity variance dominates density variance in the Arctic, this is the main cause of the trans-Arctic decrease in upper-ocean density, and hence the resulting strengthening in density gradient, which in turn increases the buoyancy frequency and hence the Rossby radius. To demonstrate this, we approximate the calculations of Eqs. (2) and (6) by setting $g = 10\,\mathrm{m\,s^{-2}}$, $\rho = 1000\,\mathrm{kg\,m^{-3}}$, $f = 1.4 \times 10^{-4}\,\mathrm{s^{-1}}$, $\mathrm{d}\rho/\mathrm{d}S = 0.8\,\mathrm{kg\,m^{-3}\,psu^{-1}}$, neglecting the impact of temperature on density, and using $\mathrm{d}z \sim H = 1000\,\mathrm{m}$ as a scale depth. Equation (5) helps to understand this last choice: the density stratification is very weak below ~1000 m, and the vertical integral of N is thus dominated by the stratification above 1000 m. The four deep Arctic Ocean basins have deep salinity ~34.8 and upper ocean salinities ca. 33.2, 31.9, 31.1 and 25.1, for the Nansen, Amundsen, Makarov, Canadian Basins respectively (see Carmack, 2000). These values translate into vertical density gradients $\sim(1\text{–}8) \times 10^{-3}\,\mathrm{kg\,m^{-4}}$, and then to buoyancy frequencies $\sim(4\text{–}9) \times 10^{-3}\,\mathrm{s^{-1}}$. Finally we obtain values of R_1 of 8, 11, 12 and 20 km (respectively), in reasonable agreement with the results shown in Figs. 5–6.

Extending the illustration to the Siberian Shelf Seas – in particular, the East Siberian Sea (Münchow et al., 1999) – we set the scale depth to 50 m and the surface-to-bottom salinity difference to 2, and obtain $R_1 = 2$ km, again in agreement with Figs. 5–6. This low value of R_1 contrasts with the deep basin values described above. The density gra-

OSD
10, 1807–1831, 2013

dient is higher, at 32×10^{-3} kg m^{-4}, and so consequently is the buoyancy frequency, at 18×10^{-3} s^{-1}. The approximate form of Eq. (6) shows that the small resulting value of R_1 is largely due to the small value of "full ocean depth" – around 50 m. With homogenisation of the water column (directly or indirectly) through winter heat loss, the vertical density gradient can assume very small values such that the shelf R_1 can decrease as low as O (100 m). This presents a challenge to observations and models alike, given the importance of the shelf seas to Arctic freshwater fluxes and water mass structure, and thereby to local and non-local climate.

We also consider the central Greenland Sea (Karstensen et al., 2005). With a surface-to-bottom (potential) density difference of ~0.1 kg m^{-3} and a scale depth of 3000 m, we find a buoyancy frequency of 0.6×10^{-3} s^{-1} and $R_1 \sim 4$ km, again in reasonable agreement with our previous results. This very low value in a deep ocean region is the result of the weak stratification that pertains throughout the water column. Several publications have described "sub-mesoscale convective vortices" found in the Greenland Sea (eg. Gascard et al., 2002; Wadhams et al., 2002; Budeus et al., 2004), and these features have radii ca. 5 km. It appears that these are not, in fact sub-mesoscale but mesoscale; it so happens that the mesoscale in this basin is very small.

As implied above, there is little in the published literature with which to compare our results. However, Saenko (2006) describes global wave speeds and Rossby radii calculated from an ensemble of coarse (~1° by 1°) resolution climate models up to 85° N using the WKBJ/LG approximation, presented as zonal means, and we parallel this style of presentation in Fig. 10, which shows our modes 1 and 2 summer and winter zonal means of wave speeds and Rossby radii. Seasonality has little impact on wave speeds by this metric. Broadly (for mode 1) we see speeds ~0.8 m s^{-1} up to ~75° N, after which, they increase steadily to over 1.6 m s^{-1} in the vicinity of the North Pole. This behaviour translates into mode 1 Rossby radii which increase from a minimum of ~2 km around 65° N to a maximum of over 11 km near the North Pole. The results of Saenko (2006) bear some similarities to this. Wave speeds compare well, albeit with some scatter, and models with the smallest mean Rossby radii are in

OSD
10, 1807–1831, 2013

agreement with ours, but several others show substantial latitudinally-dependent overestimates. In the Arctic, the zonal mean is a confused metric, which will comprise for most latitude circles south of about 84° N a mixture of shelf seas and deep ocean, with their concomitant very different conditions. Therefore it is not possible to comment further on possible sources of error in the climate models without knowing more about individual model configurations and (at least) the difference between deep ocean and shelf sea behaviour. Nevertheless, it is encouraging that some models appear to be capable of producing sensible vertical density stratification (in the zonal mean).

3.4 Observed eddies

There have in the past been several high-resolution surveys of Arctic Ocean eddies, reported in Newton et al. (1974), Hunkins (1974), Manley and Hunkins (1985), D'Asaro (1988), Padman et al. (1990), Muench et al. (2000), Pickart et al. (2005), Timmermans et al. (2008), Nishino et al. (2011) and Kawaguchi et al. (2012), and stemming (variously) from field programmes such as the Arctic Ice Dynamics Joint Experiment (AIDJEX) in the 1970s, the Arctic Internal Wave Experiment (AIWEX) in 1985, Scientific Ice Expedition (SCICEX) measurements from the 1990s, the Western Arctic Shelf-Basin Interaction (SBI) programme of 2005, Ice-Tethered Profilers (ITPs), and an expedition on the R/V *Mirai* in 2010. Curiously, all these papers report on eddies observed in the Canada Basin. It is not clear whether the Canada Basin is "infested" with eddies, or (rather) whether there is simply a paucity of eddy-resolving measurements in the other basins, caused by the difficulty of making such measurements given the ice cover.

Still, these cited observations are all more-or-less consistent in how they describe the observations. The eddy has a core where rotation is (close to) solid-body, and the outer edge of the core defines the radius of maximum velocity. Further outwards from the edge of the core is a region which is still rotating but where the velocity progressively reduces, out to a "maximum radius of influence". A typical radius conforming to the core is ∼7 km, and a typical maximum radius of influence is ∼15 km. An empirical quantification of this description is given by Timmermans et al. (2008). However,

OSD
10, 1807–1831, 2013

the eddy described by Kawaguchi et al. (2012) was (apparently) an unusually large one. Its radius was 30 km, of which the inner 15 km was in solid-body rotation and the outer 15 km comprised the penumbra. This is consistent with the local Mode 1 Rossby radius and the eddy being sufficiently removed from its generation region that it has spun up a "penumbra", so the qualitative description is still broadly consistent with the observations.

Many of the observed eddies are sub-surface and may therefore be considered as mode 2 features, which allows for small radii. Furthermore, Chelton et al. (2011) note that observed eddies may be two or three times larger than the Rossby radius. The observed Arctic eddies are, therefore, reasonable in scale – in principle. It may be possible to develop an explanation of these observations by pursuing the approach of Hoskins et al. (1985), whereby an eddy, at its point of generation (which may be via baroclinic instability) is in solid-body rotation. Subsequently the closed-contour potential vorticity anomaly induces flow in the surrounding volume, or penumbra. However, this is beyond the scope of the present manuscript.

3.5 Final remarks

Having described in the Introduction a generic model-based justification for interest in the Rossby radius, we note here some reasons for measurement-based interest. Timmermans et al. (2008) demonstrate the feasibility of making quasi-Lagrangian observations of Arctic Ocean eddies with ice-tethered profilers, but Eulerian measurements present a challenge. The only sustained Arctic Ocean measurement programme to resolve successfully the local Rossby radius is found north of Alaska (Nikopoulos et al., 2009) with a typical mooring spacing of ~5 km. Furthermore, the logistical and operational constraints of trans-polar hydrographic sections conducted on research icebreakers mean that they cannot get close to resolving the Rossby radius (eg. Carmack et al., 1997).

The Shelf Break Branch of the Arctic Circumpolar Boundary Current has only recently been described (Aksenov et al., 2011). This is a shallow feature transporting

OSD
10, 1807–1831, 2013

halocline waters that circuits most of the Arctic Ocean. Over the shelfbreak the Rossby radius is typically ∼7 km, so this current is sufficiently narrow that it had slipped almost unnoticed between more widely-spaced standard measurement locations. The model study inspired re-analysis of past measurements, and deliberate targeting of new measurements. We conclude by observing that advances in understanding of Arctic Ocean circulation and dynamics will likely be found from measurements and models in combination.

Acknowledgements. This study was funded by the UK Natural Environment Research Council, and is a contribution to to the UK TEA-COSI project. Calculations were performed with the SciPy open source python package (http://www.scipy.org).

References

Aksenov, Y., Bacon, S., Coward, A. C., and Nurser, A. J. G.: The North Atlantic Inflow into the Nordic Seas and Arctic Ocean: a high-resolution model study, J. Marine Syst., 79, 1–22, 2010a.

Aksenov, Y., Bacon, S., Coward, A. C., and Holliday, N. P.: Polar outflow from the Arctic Ocean: a high-resolution model study, J. Marine Syst., 83, 14–37, doi:10.1016/j.jmarsys.2010.06.007, 2010b.

Aksenov, Y., Ivanov, V. V., Nurser, A. J. G., Bacon, S., Polyakov, I. V., Coward, A. C., Naveira Garabato, A. C., and Beszczynska-Moeller, A.: The Arctic circumpolar boundary current. J. Geophys. Res., 116, C09017, doi:10.1029/2010JC006637, 2011.

Anderson, L. G., Björk, G., Holby, O., Jones, E. P., Kattner, G., Koltermann, K. P., Liljeblad, B., Lindegren, R., Rudels, B., and Swift, J.: Water masses and circulation in the Eurasian Basin: results from the *Oden* 91 expedition, J. Geophys. Res., 99, 3273–3283, 1994.

Budeus, G., Cisewski, B., Ronski, S., Dietrich, D., and Weitere, M.: Structure and effects of a long lived vortex in the Greenland Sea, Geophys. Res. Lett., 31, L05304, doi:10.1029/2003GL017983, 2004.

Carmack, E. C.: The freshwater budget of the Arctic Ocean: sources, storage and sinks, in: The Freshwater Budget of the Arctic Ocean, edited by: Lewis, E. L., NATO Advanced Research Series, 91–126, 2000.

OSD
10, 1807–1831, 2013

Carmack, E. C., Aagaard, K., Swift, J. H., Macdonald, R. W., McLaughlin, F. A., Jones, E. P., Perkin, R. G., Smith, J. N., Ellis, K. M., and Killius, L. R.: Changes in temperature and tracer distributions within the Arctic Ocean: results from the 1994 Arctic Ocean section, Deep-Sea Res. Pt. II, 44, 1487–1502, 1997.

Chelton, D. B., de Szoeke, R. A., Schlax, M. G., El Naggar, K., and Siwertz, N.: Geographical variability of the first baroclinic Rossby radius of deformation, J. Phys. Oceanogr., 28, 433–459, 1998.

D'Asaro, E. A.: Observations of small eddies in the Beaufort Sea, J. Geophys. Res., 93, 6669–6684, 1988.

Gascard, J.-C., Watson, A. J., Messias, M.-J., Olsson, K. A., Johannessen, J., and Simonsen, K.: Long-lived vortices as a mode of deep ventilation in the Greenland Sea, Nature, 416, 525–527, 2002.

Gill, A. E.: Atmosphere–Ocean Dynamics, Academic Press, 662 pp., 1982.

Hoskins, B. J., McIntyre, M. E., and Robertson, A. W.: On the use and significance of isentropic potential vorticity maps, Q. J. Roy. Meteor. Soc., 111, 877–946, 1985.

Hunkins, K. L.: Subsurface eddies in the Arctic Ocean, Deep-Sea Res., 21, 1017–1033, 1974.

Jakobsson, M., Cherkis, N., Woodward, J., Macnab, R., and Coakley, B.: New grid of Arctic bathymetry aids scientists and mapmakers, Eos Trans. AGU, 81, 89–96, 2000.

Karstensen, J., Schlosser, P., Wallace, D. W. R., Bullister, J. L., and Blindheim, J.: Water mass transformation in the Greenland Sea during the 1990s, J. Geophys. Res., 110, C07022, doi:10.1029/2004JC002510, 2005.

Kawaguchi, Y., Itoh, M., and Nishino, S.: Detailed survey of a large baroclinic eddy with extremely high temperatures in the western Canada Basin, Deep-Sea Res. Pt. I, 66, 90–102, 2012.

Killworth, P. D. and Blundell, J. R.: The effect of bottom topography on the speed of long extratropical planetary waves, J. Phys. Oceanogr., 29, 433–459, 1999.

Manley, T. O. and Hunkins, K.: Mesoscale eddies of the Arctic Ocean, J. Geophys. Res., 90, 4911–4930, 1985.

Marsh, R., de Cuevas, B. A., Coward, A. C., Jacquin, J., Hirschi, J.-M., Aksenov, Y., Nurser, A. J. G., and Josey, S. A.: Recent changes in the North Atlantic circulation simulated with eddy-permitting and eddy-resolving ocean models, Ocean Model., 28, 226–239, 2009.

OSD
10, 1807–1831, 2013

Muench, R. D., Gunn, J. T., Whitledge, T. E., Schlosser, P., and Smethie Jr., W.: An Arctic cold core eddy, J. Geophys. Res., 105, 23997–24006, 2000.
Münchow, A., Weingartner, T. J., and Cooper, L. W.: The summer hydrography and surface circulation of the East Siberian Shelf Sea, J. Phys. Oceanogr., 29, 2167–2182, 1999.
Newton, J. L., Aagaard, K., and Coachman, L. K.: Baroclinic eddies in the Arctic Ocean, Deep-Sea Res., 21, 707–719, 1974.
Nikopoulos, A., Pickart, R. S., Fratantoni, P. S., Shimada, K., Torres, D. J., and Jones, E. P.: The Western Arctic boundary current at 152° W: structure, variability and transport, Deep-Sea Res. Pt. II, 56, 1164–1181, doi:10.1016/j.dsr2.2008.10.014, 2009.
Nishino, S., Itoh, M., Kawaguchi, Y., Kikuchi, T., and Aoyama, M.: Impact of an unusually large warm-core eddy on distributions of nutrients and phytoplankton in the Southwestern Canada Basin during late summer/early fall 2010, Geophys. Res. Lett., 38, L16602, doi:10.1029/2011GL047885, 2011.
Padman, L., Levine, M., Dillon, T., Morison, J., and Pinkel, R.: Hydrography and microstructure of an Arctic cyclonic eddy, J. Geophys. Res., 95, 9411–9420, 1990.
Pickart, R. S., Weingartner, T. J., Pratt, L. J., Zimmermann, S., and Torres, D. J.: Flow of winter-transformed Pacific water into the western Arctic, Deep-Sea Res. Pt. II, 52, 3175–3198, 2005.
Proshutinsky, A., Krishfield, R., Timmermans, M.-L., Toole, J., Carmack, E., McLaughlin, F., Williams, W. J., Zimmermann, S., Itoh, M., and Shimada, K.: Beaufort Gyre freshwater reservoir: state and variability from observations, J. Geophys. Res., 114, C00A10, doi:10.1029/2008JC005104, 2009.
Saenko, O. A.: Influence of global warming on baroclinic Rossby radius in the ocean: a model intercomparison, J. Climate, 19, 1354–1360, 2006.
Smith, W. H. F. and Sandwell, D. T.: Global seafloor topography from satellite altimetry and ship depth soundings, Science, 277, 1957–1962, 1997.
Steele, M., Morley, R., and Ermold, W.: PHC: A global ocean hydrography with a high quality Arctic Ocean, J. Climate, 14, 2079–2087, 2001.
Timmermans, M.-L., Toole, J., Proshutinsky, A., Krishfield, R., and Plueddemann, A.: Eddies in the Canada Basin, Arctic Ocean, observed from ice-tethered profilers, J. Phys. Oceanogr., 38, 133–145, 2008.
Wadhams, P., Holfort, J., Hansen, E., and Wilkinson, J. P.: A deep convective chimney in the winter Greenland Sea, Geophys. Res. Lett., 29, 1434, doi:10.1029/2001GL014306, 2002.

OSD
10, 1807–1831, 2013

Table 1. Regional averages of Rossby radii modes 1 and 2 for winter and summer months. The tabulated regions are shown in Fig. 4, to which the key numbers refer.

Location	Key	Mode 1 (km)		Mode 2 (km)	
		Mar 1992	Aug 1992	Mar 1992	Aug 1992
Deep Arctic Ocean:					
Amerasian Basin	1	11.7	11.7	5.3	5.2
Eurasian Basin	2	8.4	8.4	4.6	4.7
Environs of Canadian waters:					
Canadian Archipelago	3	3.0	3.6	1.4	1.8
Hudson Bay & Foxe Basin	4	3.8	4.2	1.7	2.0
Baffin Bay	5	4.1	4.8	2.0	2.6
Nordic Seas:					
Greenland Sea	6	5.3	5.5	2.4	2.9
Iceland Sea	7	4.4	5.0	1.4	2.1
Norwegian Sea	8	5.7	6.5	1.9	2.6
Eurasian Shelf Seas:					
Barents Sea	9	1.0	2.6	0.4	1.2
White Sea	10	1.4	3.2	0.5	1.4
Kara Sea	11	2.4	3.1	1.1	1.4
Siberian Shelf Seas	12	1.5	2.6	0.7	1.1

OSD
10, 1807–1831, 2013

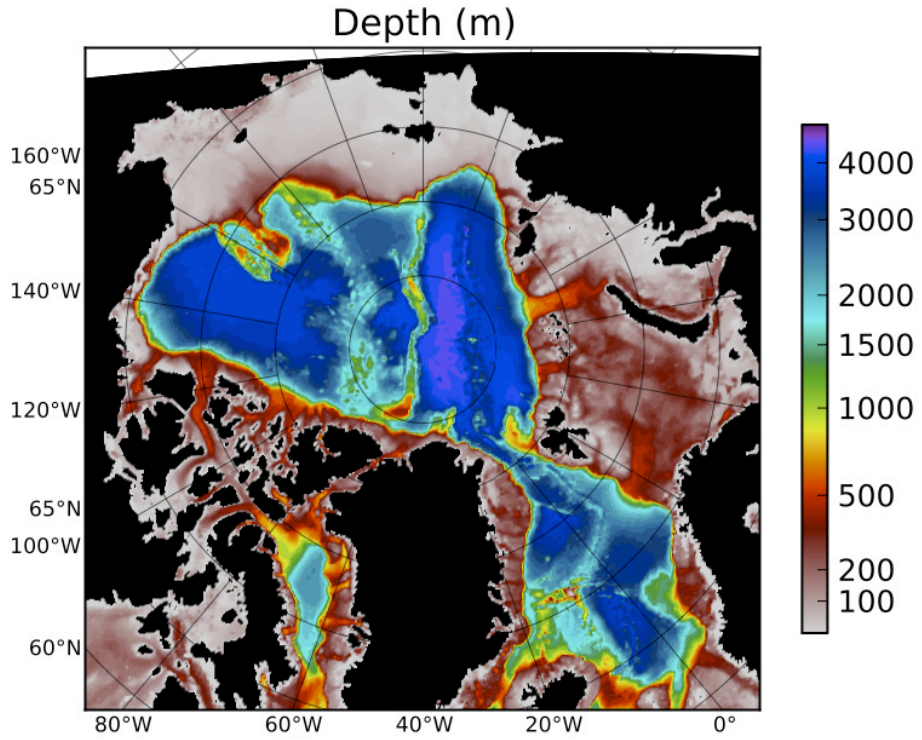

Fig. 1. OCCAM model bathymetry (m).

OSD
10, 1807–1831, 2013

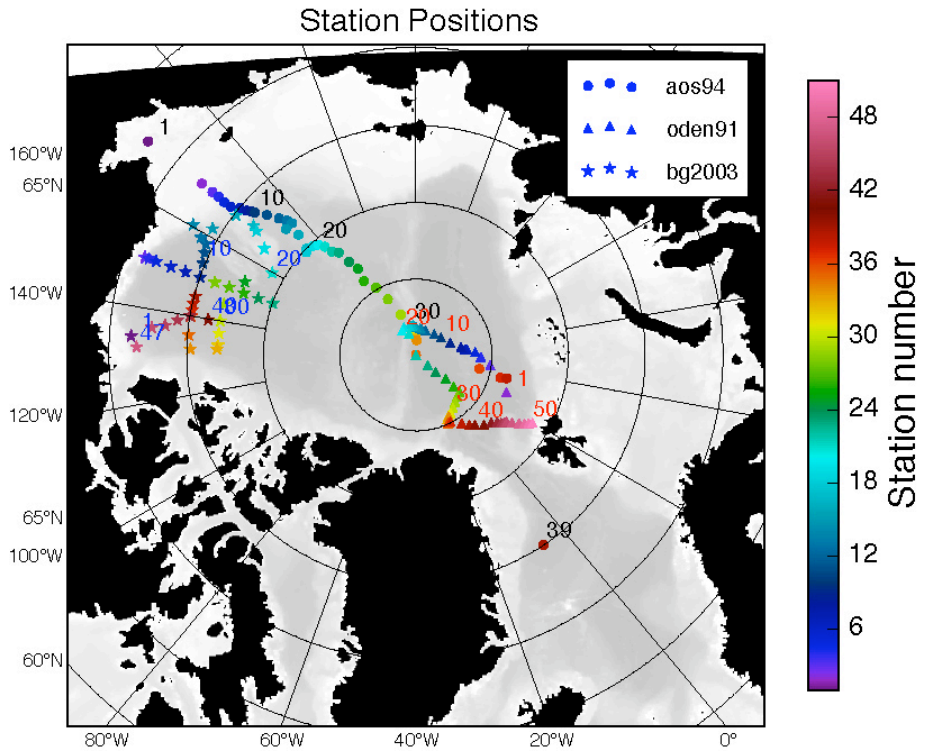

Fig. 2. Station locations. Expeditions are identified by symbol in the key, where aos94 is Arctic Ocean Section 1994, oden91 is the Oden 1991 section, and bg2003 is the Beaufort Gyre survey of 2003. Station numbers are coloured (see scale bar). The background is topography in grey-scale. See text (Sect. 2) for further details.

OSD
10, 1807–1831, 2013

(a)

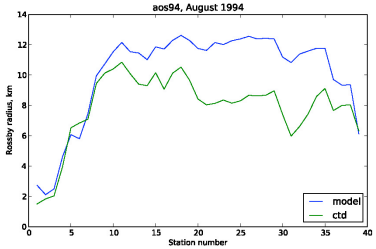

(b)

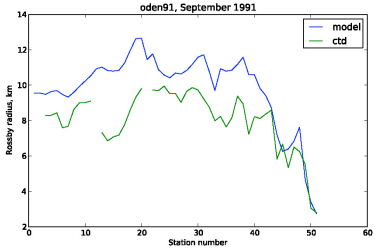

(c)

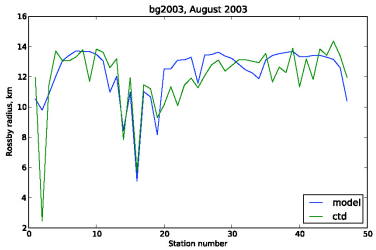

Fig. 3. Comparison of exact Rossby radii calculated from the model and the data: **(a)** AOS'94; **(b)** Oden'91; **(c)** BGEP 2003.

OSD
10, 1807–1831, 2013

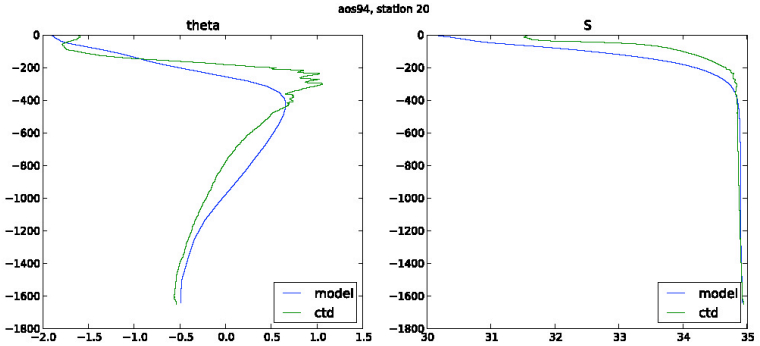

(a)

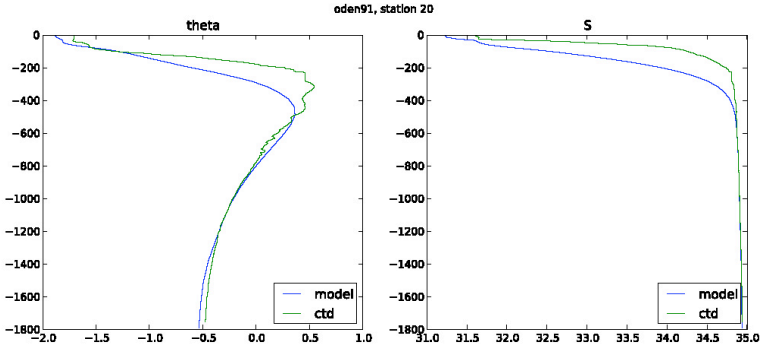

(b)

Fig. 4. Comparison of co-located model and data temperature and salinity profiles: **(a)** AOS'94, station 20; **(b)** Oden'91, station 20.

OSD
10, 1807–1831, 2013

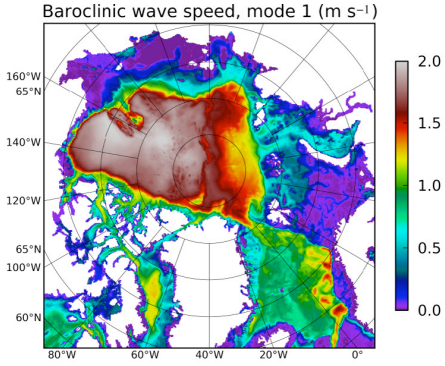

(a)

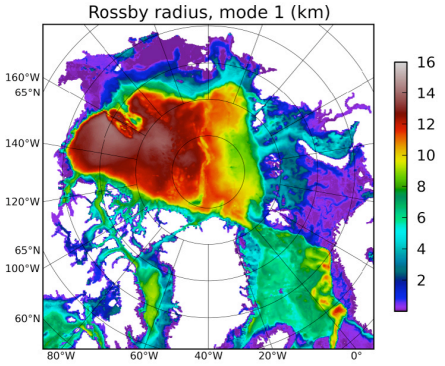

(b)

Fig. 5. (a) baroclinic wave speed (m s^{-1}) mode 1, March 1992; **(b)** Rossby radius (km) mode 1, March 1992.

OSD
10, 1807–1831, 2013

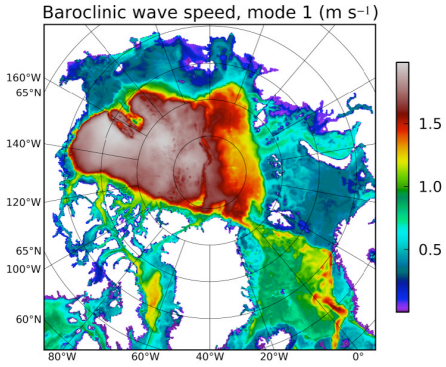

(a)

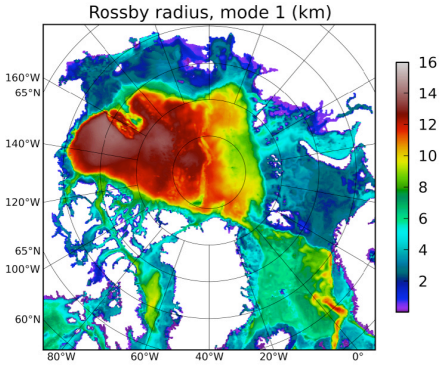

(d)

Fig. 6. (a) baroclinic wave speed (m s^{-1}) mode 1, August 1992; **(b)** Rossby radius (km) mode 1, August 1992.

OSD
10, 1807–1831, 2013

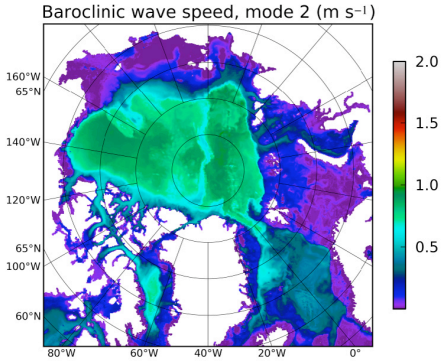

(a)

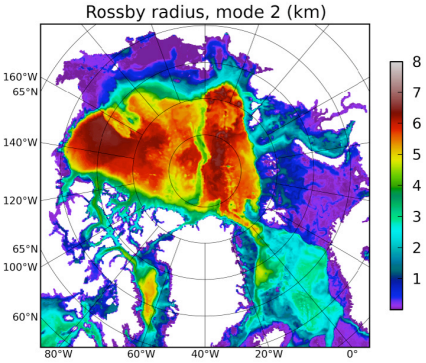

(b)

Fig. 7. (a) baroclinic wave speed (m s^{-1}) mode 2, March 1992; **(b)** Rossby radius (km) mode 2, March 1992.

OSD
10, 1807–1831, 2013

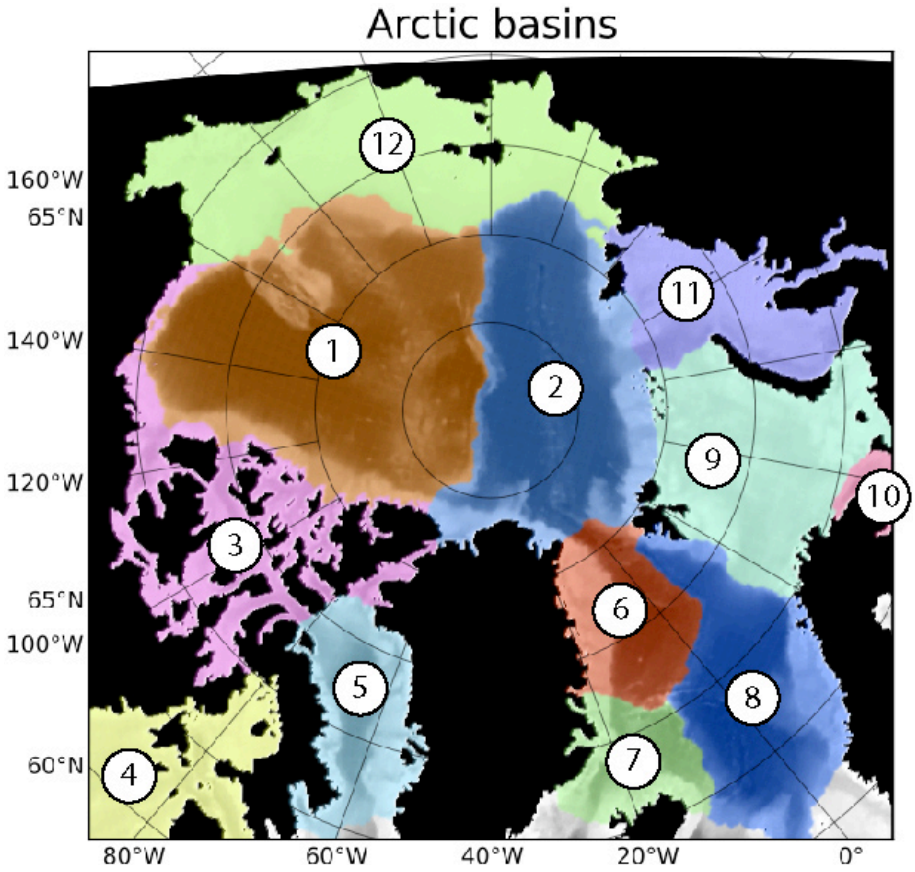

Fig. 8. Division of Arctic Ocean regions for average wave speed and Rossby radius calculations; see Table 1 for identification of sub-regions by key number.

OSD
10, 1807–1831, 2013

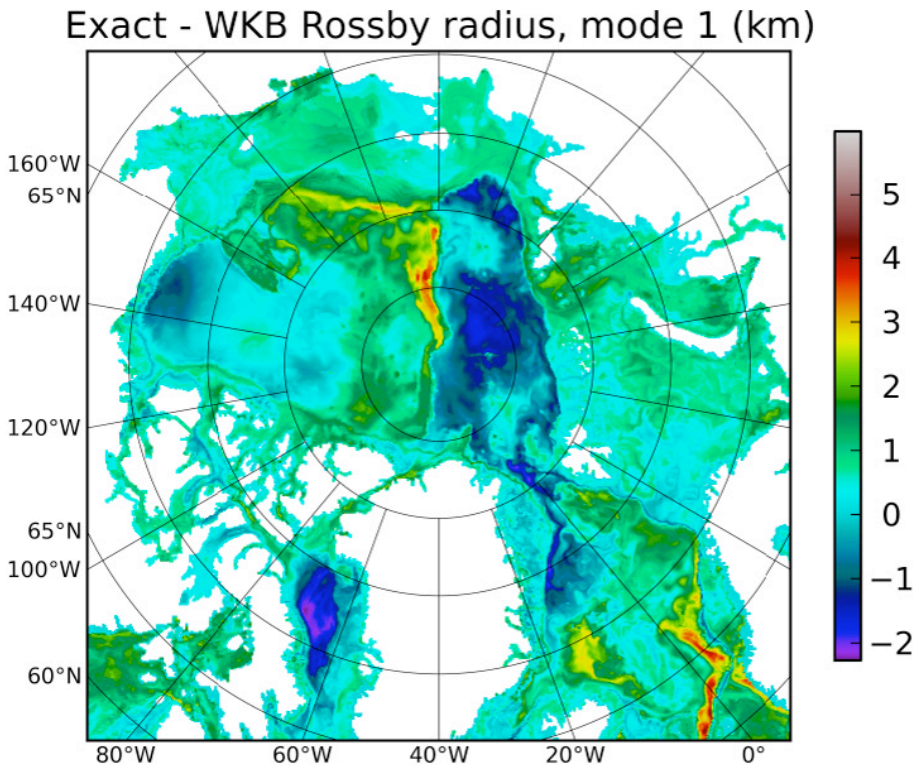

Fig. 9. Difference between exact solution and WKB approximate solution (exact minus WKB) for August 1992 mode 1 Rossby radius (km).

OSD
10, 1807–1831, 2013

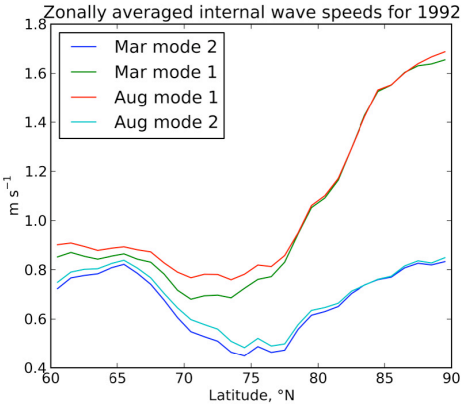

Fig. 10. Zonal means for Rossby radii modes 1 and 2 for March and August 1992, of **(a)** wave speed (m s^{-1}), and **(b)** Rossby radius (km).

OSD
10, 1807–1831, 2013